

Celestial Choreography: Turbulence's Influence on Dust Clouds in the Heart of
NGC 628

A Thesis
Presented to
The Division of Mathematics and Natural Sciences
Reed College

In Partial Fulfillment
of the Requirements for the Degree
Bachelor of Arts

Unda O. March
December 2023

Approved for the Committee
(Physics)

Alison Crocker

Acknowledgements

To the countless people who have been my guiding lights throughout my college journey, a heartfelt thank you. Your support, whether in academic realms or navigating uncharted territories as a first generation student, has been invaluable. To my amazing friends and chosen family in DC and Portland and everywhere in between, thank you for choosing me every day and being my pillars of strength especially to Jenny, Christian, Shelby, and Anthony.

I am grateful to the current and former Reed staff, including but not limited to Jessika Chi, Steve Abrâhao, Tawana Parks, and the team at CLBR. Additionally, I deeply appreciate the guidance and support from my KIPP Forward counselor, Ashley Mendoza, and the foundation Data Team. I want to thank my thesis advisor Alison Crocker and readers Darrell Schroeter, Catherine Witt, and Thomas Dannenhoffer-Lafage, and of course advisor and advocate Mark Beck. Finally, I would like to thank my music teacher, John Vergin, for helping me find my voice.

It really takes a village.

Table of Contents

| | |
|--|-----------|
| Chapter 1: Introduction | 1 |
| 1.1 Galaxies and their Interstellar Matter | 1 |
| 1.2 An introduction to turbulence | 1 |
| 1.3 The relevance of turbulence | 2 |
| 1.4 Previous measurements of turbulence | 4 |
| Chapter 2: Methods and Observations | 5 |
| 2.1 Image Source | 5 |
| 2.2 Dust Cloud Counting | 5 |
| 2.2.1 Box Counting and Cloud Counting | 6 |
| 2.2.2 Unsharp Masking | 7 |
| 2.2.3 Azimuthal Scans | 7 |
| 2.2.4 Fractal Dimension | 10 |
| 2.2.5 Discussion | 10 |
| 2.3 Fourier Transform Power Spectra | 11 |
| 2.3.1 Computational Method | 12 |
| 2.3.2 Fourier Transform Power Spectra | 13 |
| 2.3.3 Discussion | 13 |
| Conclusion | 17 |
| Appendix A: Appendix | 19 |
| A.1 Azimuthal Scans | 19 |
| A.2 Dust Spiral Counts | 26 |
| Bibliography | 29 |

Abstract

The structure of dust spirals in NGC 628 is observed using James Webb Space Telescope image data to demonstrate turbulence as a factor in the galaxy's star formation processes. A cloud counting method yields a fractal dimension of $D = 0.69 \pm 0.04$, akin to turbulence influenced galactic disks. An analysis of the image's FFT power spectra reveals slopes approximating $-5/3$ for larger radii, indicative of turbulence driven patterns. Smaller radii deviations hint at diverse structural behaviors. These findings highlight turbulence as a driving force in shaping NGC 628's structure.

For Neptune

Introduction

1.1 Galaxies and their Interstellar Matter

NGC 628, also known as Messier 74, lies 32 million light years (9.77 Mpc) [1] away in the Pisces constellation. Its unique star formation hints at insights into the broader structure and evolution of galaxies in our universe. To unravel the mysteries within NGC 628, we begin by studying the Milky Way, a similar spiral galaxy, setting the stage for our exploration into cosmic turbulence.

Our home galaxy encompasses three primary components: the disk, the central bulge, and the Galactic halo [2]. The galactic disk, situated within a rich expanse of gas and dust and boasting a scale-height of approximately 100 parsecs, serves as an active nursery for stars. Its elder counterpart, the older thin disk, extends over a span of about 325 parsecs. Additionally, the thick disk, characterized by a scale-height of 1.5 kiloparsecs [2], makes a more modest contribution to the overall mass density within the galactic plane. Within the spiral arms, dense and cool molecular clouds, abundant with molecular formations, serve as stellar nurseries for emerging stars. These clouds contract under gravity's influence, birthing stars amidst regions painted blue by youthful stars and HII-regions [2]. This activity not only spawns open star clusters, but also highlights their cyclical nature. Upon reaching the end of their lives, they return their material to the cosmos in the form of gas and dust, contributing to the replenishment of interstellar matter within its medium.

In galaxies like the Milky Way, star formation is a fundamental process that occurs within regions of immense gas and dust, driven by physical mechanisms such as gravitational collapse, shock waves, and turbulence. Within this galactic context, star formation plays a pivotal role in shaping the composition and evolution of the stellar population. However, this cosmic interplay is anything but stagnant. Turbulence, like an invisible conductor, shapes the movement of gas and dust clouds and holds profound implications for the formation of stars.

1.2 An introduction to turbulence

Turbulence plays a crucial role in many natural and engineered systems, including fluid flow in the atmosphere, oceans, and even within galaxies like the Milky Way. It

is a phenomenon characterized by chaotic and irregular motion within a fluid [3] and exhibits unpredictability in space and time, making it a form of chaos. What sets turbulence apart is its ability to generate randomness on its own. Even though the governing equations are deterministic, turbulence emerges due to extreme sensitivity to disturbances, whether from initial conditions, boundary conditions, or external influences. It has the ability to significantly amplify its effects on an immense cosmic scale [3].

Fluid flow in a pipe serves as a common example of turbulence. The predictability of this behavior is governed by the Reynolds number Re , a dimensionless value expressing the ratio between inertial and viscous forces. When fluids with higher viscosity move through a pipe, they exhibit a more ordered, sluggish flow. This behavior, akin to substances like honey, shows less mixing between fluid layers, particularly at low velocities or in smaller pipes. The forces driving the fluid are relatively weak compared to the resisting forces of viscosity, resulting in a predictable, uniform flow with minimal turbulence. This behavior characterizes a low Reynolds number. For a fluid moving with velocity u through a pipe of diameter d , and kinematic viscosity v shown in Equation 1 [4]:

$$Re = \frac{ud}{v}. \quad (1.1)$$

Absolute, or dynamic viscosity, is defined as the tangential force per unit area required to slide one layer against another [5], or the relationship between the shear stress (F/A) and velocity gradient (dv_x/dz) in a fluid [6]:

$$\eta = \frac{F/A}{dv_x/dz}. \quad (1.2)$$

Kinematic velocity is then the absolute velocity over the density of the fluid [5]

$$v = \frac{\eta}{\rho}. \quad (1.3)$$

At a low Reynolds number, laminar flow (as described above) will occur where the viscous forces are dominant. Fluid particles move smoothly along non-intersecting paths, with each one tracing the trajectory of the particle preceding it. At a high Reynolds number, where inertial forces become dominant, turbulent flow occurs.

Figures 1.1 and 1.2 depict two examples of turbulent flow. Figure 1.1 highlights the distinction between laminar and turbulent flow. Figure 1.2 illustrates the scales at which turbulent flow occur which is essential to our understanding of the formation of dust clouds and, consequently, stars, within spiral galaxies.

1.3 The relevance of turbulence

Turbulence within interstellar environments spans a vast range of scales, from immense structures like supernova remnants or galactic arms down to much smaller scales such as molecular clouds or filaments. The Richardson cascade concept serves

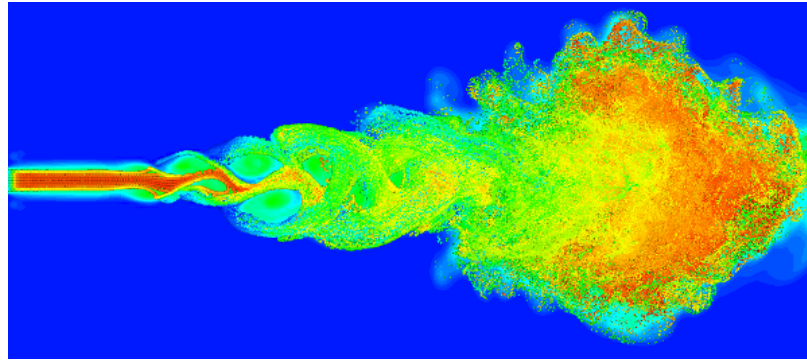


Figure 1.1: The transition from laminar (smooth) to turbulent flow. This shift may occur due to increased fluid velocities surpassing critical values, disruptions caused by rough surfaces or obstacles within the flow, and instabilities triggered by changes in fluid properties or external forces. Photo by Yale University.

as a guiding principle, illustrating the transfer of energy across these scales in turbulent flows. It demonstrates how larger turbulent motions impart energy to smaller eddies and structures. This cascading transfer continues until the energy dissipates at the smallest scales due to the effects of viscosity, echoing Richardson's insight that "big whirls have little whirls which feed on their velocity...and so on to viscosity."^[7] This energy transfer between scales in turbulent flows is essential to the shaping distribution, dynamics, and evolution of interstellar matter within galaxies.

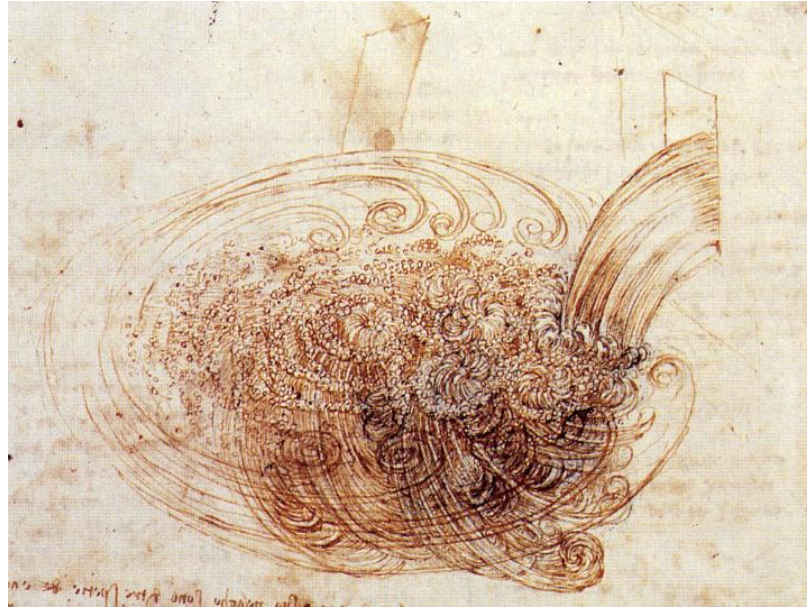


Figure 1.2: da Vinci's "whirls within whirls". Photo by Yale University.

In 1951, von Weizsäcker proposed a theory for interstellar matter similar to current understanding. It suggests that cloudy structures form hierarchical arrangements through supersonic turbulence within interacting shock waves. These turbulent pro-

cesses are primarily driven by energy sources such as galactic rotation, stellar feedback, and magnetic fields on a large scale and are dissipated by atomic viscosity on a smaller scale [8]. This theory underscores the significance of comprehending turbulence's impact on galaxy and star formation.

1.4 Previous measurements of turbulence

The methods employed in this thesis are adapted from the approach used by Elmegreen et al. in their analysis of spiral galaxies NGC 4450 and NGC 4736. In their study, Elmegreen and colleagues apply two distinct techniques: cloud counting and Fast Fourier Transform on azimuthal projections around the galaxies' centers, using data from the Hubble Telescope, which captures absorption data in visible light [9]. In contrast, this thesis will focus on the distribution of dust via emission data obtained from the James Webb Space Telescope (JWST), which operates in the infrared spectrum. These adapted methods are applied to investigate turbulence within NGC 628, utilizing data from the JWST to uncover any analogous observations of turbulence.

Methods and Observations

2.1 Image Source

Using data obtained from the James Webb Space Telescope (JWST), the intricate characteristics of NGC 628 are explored. NGC 628 is nicknamed the Phantom Galaxy due to its low surface brightness, which makes the JWST, designed to operate in the infrared spectrum, suitable for exploring its properties within opaque dust clouds. The JWST's primary mirror has a diameter of 6.5 meters (21 feet 4 inches) compared to the Hubble's 2.4 meters (7 feet 10.5 inches), with each of the 18 hexagonal shaped mirror segments being 1.32 meters (4.3 feet) in diameter [10]. The telescope is sensitive from gold colored visible light to the mid-infrared spectrum, operating at wavelengths ranging from 0.6 micrometers to 28.5 micrometers [10].

The image data collected from JWST was calibrated to ensure data quality and precision and had an original pixel dimension of 5648×2092 . The JWST's Mid-Infrared Instrument (MIRI) provides image filtering from $5\mu\text{m}$ to $28\mu\text{m}$ which allows for the study of young warm exoplanets and spectroscopy of their atmospheres, identification of the first galaxies at redshifts, and the analysis of warm dust and molecular gas in proto-planetary disks around young stars. The MIRI has a single filter wheel that holds 10 filters for imaging, 4 filter-diaphragm sets for coronagraphy, and one double prism assembly for low resolution spectroscopy. The image taken for this study uses a filter of $10\mu\text{m}$. The MIRI also has a resolution spectrometer with 2 wheels for controlling gratings and dichroic positions [11]. Figure 2.1 shows a cropped image of the NGC 628 galaxy data loaded in using the Astropy Python package, displaying a range of $50 - 1100 \times 400 - 2250$ pixels.

The following analysis employs two key methodologies: running an algorithm to count dust spirals around the nucleus at different spatial scales and applying one dimensional Fast Fourier Transforms to unravel the underlying dynamics and structures of NGC 628.

2.2 Dust Cloud Counting

A dust cloud counting technique is employed to examine the image of NGC 628. This approach mirrors the methodology described in the Elmegreen et. al. investigation

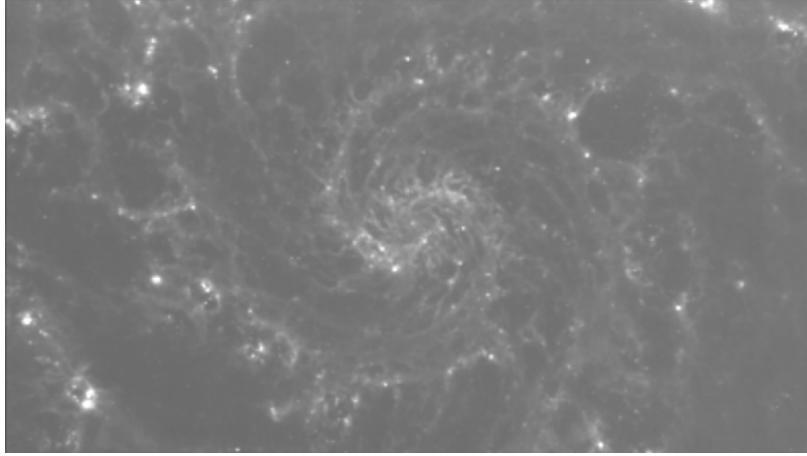


Figure 2.1: Cropped image data of NGC 628 (Messier 74) obtained by the James Webb Space Telescope (JWST).

of galaxies NGC 4450 and NGC 4736, which involves counting features on images with progressively larger filters to assess the fractal dimension [9]. As fractal patterns exhibit self-similarity across various scales, and turbulence presents this multi-scale characteristic, the identification of a fractal pattern aligns with the presence of turbulence within the galaxy.

2.2.1 Box Counting and Cloud Counting

Given their hierarchical scale nature, turbulent flows are expected to generate a fractal pattern [12]. The fractal dimension, which measures the rate at which the object's complexity changes as the observation scale varies, of these multi-scale structures can be determined through box counting or cloud counting methods [9].

Box counting works by dividing a data set, object, or image into box shaped pieces to be analyzed at a smaller scale. By systematically counting the number of boxes needed to cover the object or image at various scales, it becomes possible to quantify how the object's complexity changes with the scale of observation. Mathematically, it is expressed as [13]

$$N(> S) = AS^{-D} \quad (2.1)$$

where $N(> S)$ is the count of structures larger than a particular mesh spacing S , while A is a constant. The fractal dimension D is derived from the negative slope when plotting $N(> S)$ versus S on a log-log graph.

In astrophysical studies like the investigation of NGC 628, similar principles apply when assessing the distribution of dust clouds. Cloud counting involves the enumeration of progressively larger structures, such as dust clouds in astronomical images, to determine the fractal dimension of dust within galaxies. Instead of counting at a specific scale S , this method involves counting over a range of scales dS . The count $N(> S)$ of structures within this scale range is expressed as

$$N(> S) = \int_S^{\infty} n(S) dS \quad (2.2)$$

where $n(S) dS$ represents the count of structures ranging from S to $S + dS$. The relationship between the count and the size range is derived by combining equations (2.1) and (2.2) and taking the derivative [13]

$$n(S)dS = A(-D)S^{-D-1} \propto S^{-D-1}. \quad (2.3)$$

Transforming this in terms of logarithmic intervals, we arrive at [13]

$$n(S)d\log S \propto S^{-D} \log S. \quad (2.4)$$

Applying cloud counting to image data involves observing the data through filters of varying sizes. The slope resulting from the log-log plot of cloud counts at each filter size provides an estimation of the fractal dimension D for the cloud structures.

2.2.2 Unsharp Masking

The use of a filtering technique such as unsharp masking allows for the observations of the galaxy's structure at specific scales by subtracting Gaussian filtered images at close, but different σ values to draw attention to features on scales between the two. This method enhances contrasts at defined scales, making certain details more pronounced and aiding in the analysis of distinct features within the galactic structure.

In the study of NGC 628, a series of unsharped masked images were created to enhance the visibility of faint spiral dust structures. Initially, a Gaussian smoothing function with a dispersion of $\sigma = 3$ pixels was applied to the original image, resulting in the creation of the G3 image. Subsequently, the G2, G4, G8, and G16 images were generated by adjusting the smoothing function's sigma values, each increasing by powers of 2. This logarithmic approach enables the detection of consistent patterns across a wide range of scales, supporting the identification of inherent self-similarity within the galaxy's complex structures.

Following the generation of these base images, additional filtering was carried out. The G6, G12, G24, and G48 images were obtained by filtering with relevant kernel values, followed by the creation of the unsharp masked images by subtracting each base image multiplied by 3 from its respective counterpart. These subtracted filtered images, G1-G3, G2-G6, G4-G12, G8-G24, and G16-G48 exhibit a diverse array of structures as shown in Figure 2.2, illustrating the presence of spiral dust clouds across various scales.

2.2.3 Azimuthal Scans

An azimuthal scan involves the measurement of intensity of an object or field at various angular positions around a central point. In this study, azimuthal scans are used to count the number of dust structures around the galactic center.

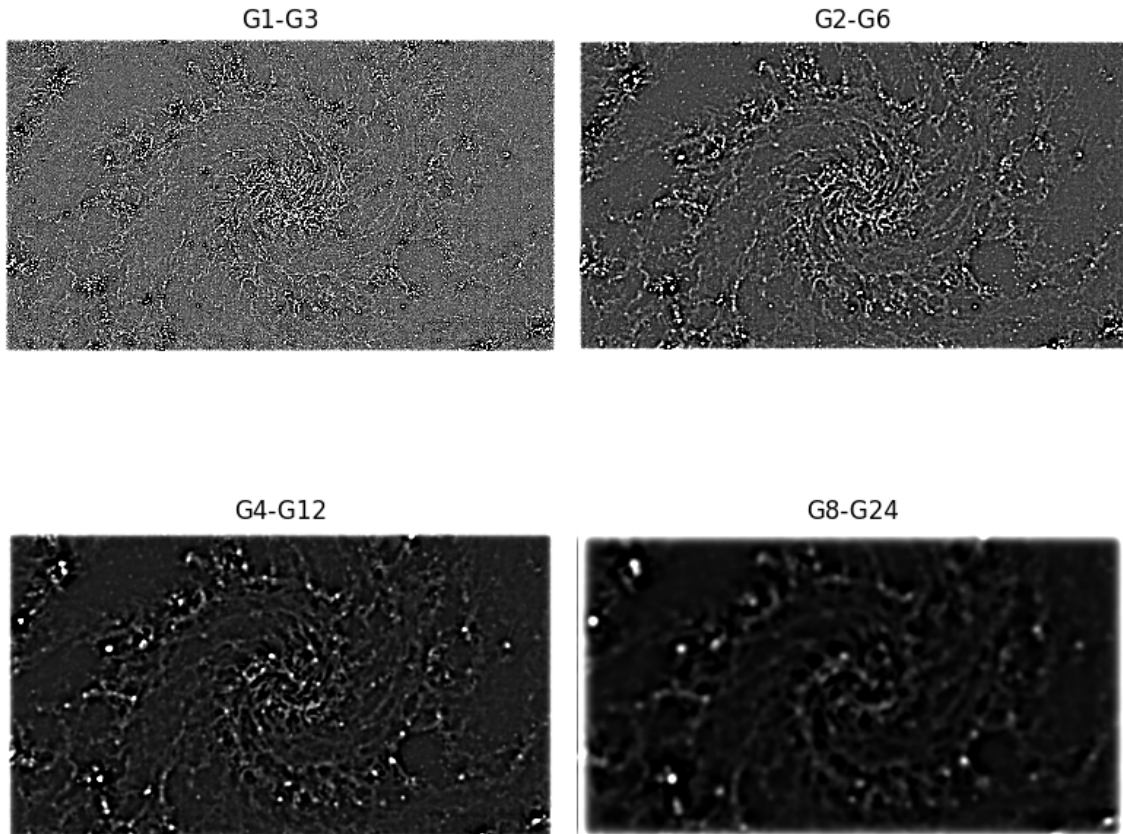


Figure 2.2: Unsharp masked images of NGC 628 show enhanced details in the galaxy’s spiral dust structures, obtained by subtracting Gaussian smoothed images with varying dispersions. Greater dispersions in the Gaussian smoothing process accentuate features on broader scales as they encompass a wider area when blurring the image, revealing the details present on larger scales in the galactic structure.

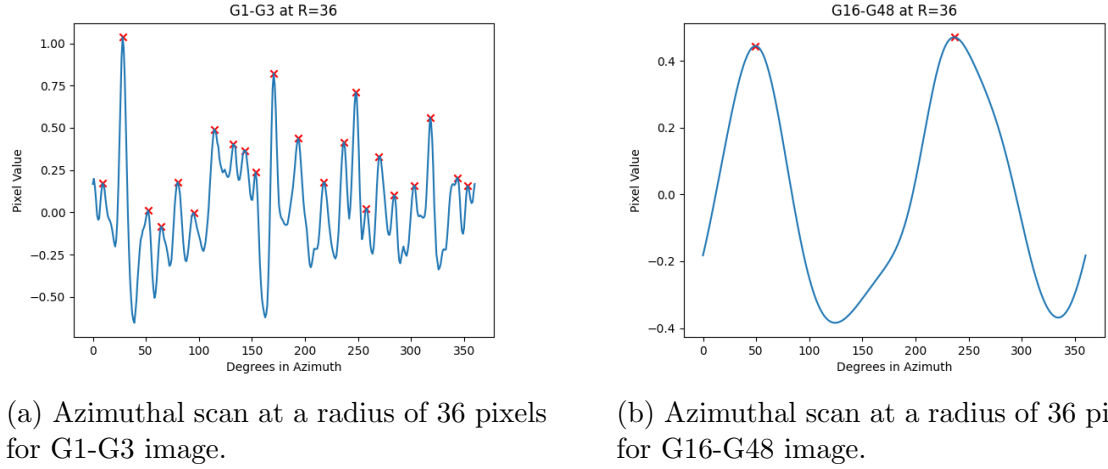


Figure 2.3: The local maxima of the plots are marked with red x's and depict the emissions as encoded pixel values around the path of the scans. The differences in the number of detected dust spirals between the two images are attributed to the varying levels of blur introduced by the unsharp masking technique. The less blurry image (G1-G3) shows numerous dust spirals, whereas the more blurred image (G16-G48) prominently displays only two faint spiral arms at the same radius.

For uniformity across the unsharp masked images, the galaxy's center was determined using the Photutils centroid function¹ applied to a 2D cutout from the original image. The function calculates the object center of mass from 2D image moments. The center is located at a point of (926.5, 522.6) pixels.

The radii used to create the azimuthal scans are 9, 18, 27, 36, 45, 55, 64, 73, 81, 91, 100, and 109 pixels. With each pixel corresponding to an angular size of 0.11 arcseconds, each step in radius represents one arcsecond. Figure 2.3 shows the azimuthal scans for the G1-G3 and G16-G48 images at a radius of 36 pixels. When filtering at smaller scales, many more dust spirals are counted since elements with higher frequencies are allowed. However, filtering at larger scales highlights only the lowest frequency components with a greater reduction in background noise, showing in Figure 2.3(b) the two main spiral arms of the galaxy.

The algorithm reads the pixel value at each degree in azimuth and outputs the value corresponding to brightness at that location, plotting it against each degree in a clockwise orientation as shown in the plots in Figure 2.3². An additional line of code imposes the markings of local maxima on each plot where the brightest points indicate the presence of dust clouds and filters out minor fluctuations by dynamically adjusting the threshold to 5% of the maximum pixel value in each azimuthal scan³. This adaptive thresholding accounts for variations in image contrast and noise,

¹Phoutils is an Astropy Python package that facilitates the detection and photometric analysis of astronomical sources.

²For each radius, the algorithm calculates azimuthal coordinates and maps pixel values to these coordinates using the `map_coordinates` function from the SciPy library.

³Local maxima in azimuthal profiles were automatically detected using Python's `find_peaks`

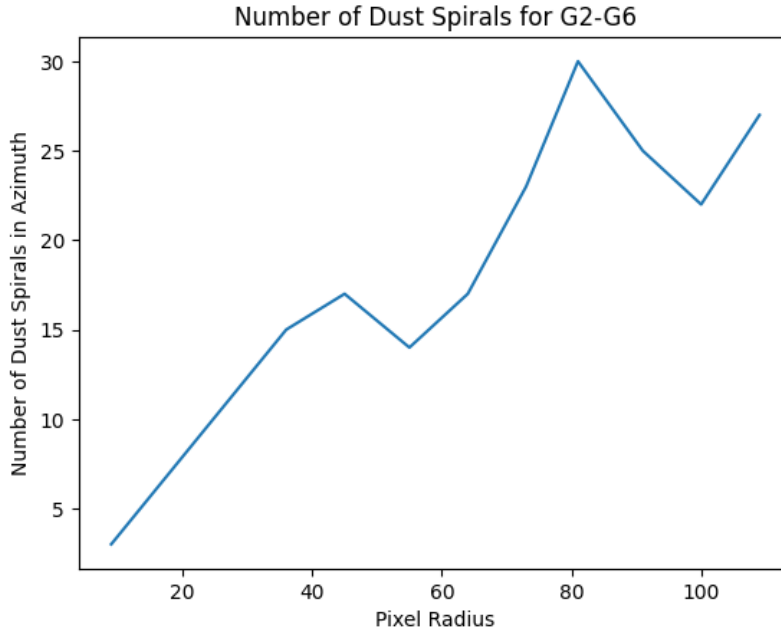


Figure 2.4: Dust spiral count across different radii for the G2-G6 image.

enhancing the accuracy of peak detection by highlighting only the brightest points as local maxima. The process was applied to each image difference and radius. The appendix contains the scans for the G8-G24 image.

After marking the dust clouds, additional plots were made of each image difference to examine the correlation between the number of detected dust spirals and the radius of azimuthal projection. Figure 2.4 illustrates the count of dust spirals across various radii for the G2-G6 image.

2.2.4 Fractal Dimension

Figure 2.5 shows a plot of the log-log data of the cloud count versus each range of scales. The calculated fractal dimension is $D = 0.69 \pm 0.04$. This computation involves employing linear regression on logarithmic data, fitting a line to the log-log plot of structure counts across observation scales for each radius to determine the slope, representing the fractal dimension⁴.

2.2.5 Discussion

The calculated fractal dimension for the distribution of dust clouds in NGC 628 is found to be $D = 0.69 \pm 0.04$. Figure 2.5 shows a plot of the log-log data of the

routine from the `scipy.signal` module.

⁴The `LinearRegression` module from the `scikit-learn` library is used to fit a linear regression model to the log-log plot, determining the slope of this line. The slopes obtained from each radius' log-log plot are stored and used to calculate the average slope, representing the fractal dimension. The standard deviation across all slopes provides the error estimation for the computed fractal dimension.

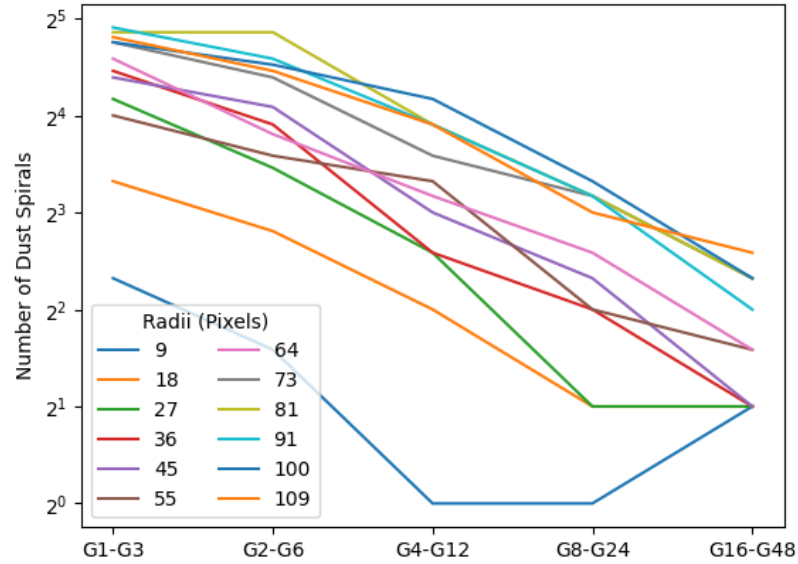


Figure 2.5: The count of distinct dust spirals recorded in azimuthal scans at various radii is correlated with the Gaussian dispersion of the unsharp mask. The spirals exhibit a power law decline in number, with a calculated fractal dimension of $D = 0.69 \pm 0.04$.

cloud count of each radius. Excluding the flatter $R = 9$ slope which has a higher cloud count than anticipated due to possible noise, the fractal dimension is found to be $D = 0.71 \pm 0.04$. This value, being close to 1, suggests a self similar and complex structure in the arrangement of dust clouds [9]. Comparing this result to prior astrophysical studies, such as that in Xie’s thesis and the Elmegreen study, reveals interesting insights. Xie’s study, with a fractal dimension of 0.488 ± 0.117 [13] for NGC 524, indicates hierarchical or fractal characteristics in interstellar clouds, reminiscent of turbulence. The Elmegreen study reports apparent fractal dimensions slightly less than 1 (0.79 ± 0.16 for NGC 4450 and 0.51 ± 0.04 for NGC 4736) [9], emphasizing the interconnected nature of cloud distribution. In this case, the fractal dimension of 0.69 implies some degree of self-similarity, pointing towards turbulent behavior that does not entirely occupy the galactic medium. While it doesn’t exhibit perfect self similarity, the value indicates a substantial degree of similarity across multiple scales. This aligns with the notion that fluctuations on different scales cascade to create a complex, turbulent environment.

2.3 Fourier Transform Power Spectra

Following the method outlined by Elmegreen et al., a one dimensional power spectrum is then conducted via a Fast Fourier Transform (FFT) algorithm to trace intensity values around the galaxy’s center. This approach allows for a breakdown of intensity variations into different spatial frequencies, enabling the identification of dominant patterns within the galactic image. By characterizing these patterns based on their

frequencies, it is then possible to understand the size distribution and prevalence of structural elements such as dust clouds or spiral arms at various scales. Furthermore, the power spectrum analysis quantifies the degree self-similarity within the image, providing insights into the presence and nature of repeating patterns across different scales in the galactic structures observed. Turbulence should demonstrate a power spectrum slope of $-5/3$ for structures thinner on the line of sight than the wavelength and $-8/3$ for structures thicker on the line of sight than the wavelength [9]. Given the orientation of this face-on galaxy, the line of sight thickness can be considered the thickness of the gaseous disk of the galaxy.

2.3.1 Computational Method

The projected circles were taken at radius values of $R = 33, 57, 81, 107, 134, 153, 185, 204, 229$, and 224 pixels. These radii were chosen to align with computational efficiency, meeting the pixel count requirements for the FFT analysis while minimizing computational complexity.

Building on previous code, the algorithm generates coordinates along circular paths around the galactic center for each new radius, extracting intensity profiles at these radial points. In order to apply the FFT analysis to the image with frequency determined with respect to space, the image is converted from pixels to spatial units.

The spatial frequency data utilized in the Fast Fourier Transform initially resided in inverse pixels, is derived from the azimuthal values representing different degrees around the circular dataset. To facilitate a conversion to inverse parsecs, the conversion from inverse pixels to inverse degrees is computed using the formula

$$\text{Inverse pixels} = \text{Inverse degrees} \times \frac{360}{2 \times \pi \times R} \quad (2.5)$$

where R represents variable radii in pixels. Then the transformation from inverse degrees to inverse parsecs was performed via

$$\text{Inverse parsecs} = \text{Inverse pixels} \times \frac{1\text{pixel}}{0.11\text{arcsecs}} \times \frac{206265\text{arcsecs}}{1\text{rad}} \times \frac{1}{D} \quad (2.6)$$

where D is the distance to the galaxy in parsecs (9.77×10^6 pc from the introductory chapter). This conversion allows visualization of the spatial frequency spectrum in units of inverse parsecs, providing an understanding of the distribution of power in the Fourier domain with respect to physical distances in space.

These profiles then undergo FFT⁵ to reveal frequency content, presenting spatial frequency distributions for various radial distances encircling the galaxy. This process

⁵The code uses NumPy's FFT function `np.fft.fft` to compute the one-dimensional n-point discrete Fourier Transform. It processes azimuthal intensity profiles sampled along concentric circles within the image, transforming the spatial domain information into the frequency domain and revealing the distribution of signal power across different spatial frequencies. The generated power spectra is used to characterize structural patterns and features present within the image.

unveils the strengths and distributions of spatial frequencies within the intensity profiles. A mask is applied to the FFT generated frequency array, extracting only the positive frequency components as negative frequency values do not contribute additional information for the analysis.

2.3.2 Fourier Transform Power Spectra

The power spectra, plotted against positive frequency values with increasing radii, are shown in Figure 2.6. They exhibit slopes to demonstrate known characteristics of turbulence. Linear regression on log-log scales calculates the slope, quantifying scaling properties and self-similarity within the galactic structures. This analysis presents spatial variations and scaling properties across radial distances around the galactic center.

2.3.3 Discussion

The power spectra analysis of NGC 628 exhibited a slope of approximately $-5/3$ for larger radii which aligns with expectations set forth in Elmegreen et al.'s study on turbulence. This slope correspondence typically signifies structures that are thinner on the line of sight than the transverse wavelength, meaning that they appear to be stretched out or extended in one direction the line of sight compared to their dimensions in the other directions. However, the deviation from this expected $-5/3$ slope for smaller radii in NGC 628 suggests a different structural behavior or scale characteristic within these regions. This discrepancy echoes observations made in Elmegreen's and Xie's studies, where deviations from the $-5/3$ slope were noted as the radii measurements shifted. Xie's thesis remarks on a similar deviation as the radius increased, indicating a flattening of the slope. This observation may indicate various factors contributing to the structure at different radial distances such as the presence of more intricate structures at smaller scales farther from the galactic center, or increased noise levels at larger radii making the structures less distinguishable.

Elmegreen et al.'s study notes a transition from a slope of $-5/3$ to $-8/3$ at high spatial frequencies, implying a change in structure size relative to the line of sight compared to the transverse wavelength. This transition in slope in high spatial frequencies reflects a change in the nature of structures within galaxies. In the context of turbulence and star formation, it suggests a shift in the underlying mechanisms shaping these structures. Structures thinner than the line of sight wavelength ($-8/3$ slope) potentially indicate regions where the gas is more compressed, possibly fostering conditions conducive to star formation. Expressed in units of inverse parsecs, this measurement might provide an estimation of the transition thickness from a power spectrum slope of $-5/3$ to $-8/3$. Meanwhile, structures thicker than the line of sight wavelength ($-5/3$ slope) might represent larger-scale turbulent motions, influencing gas dynamics without necessarily leading to immediate star formation.

While NGC 628 demonstrates an approximate $-5/3$ slope for larger radii, the discrepancy observed for smaller radii aligns with the complexities noted in Elmegreen's findings, suggesting a possible change in scale behavior or structural characteristics

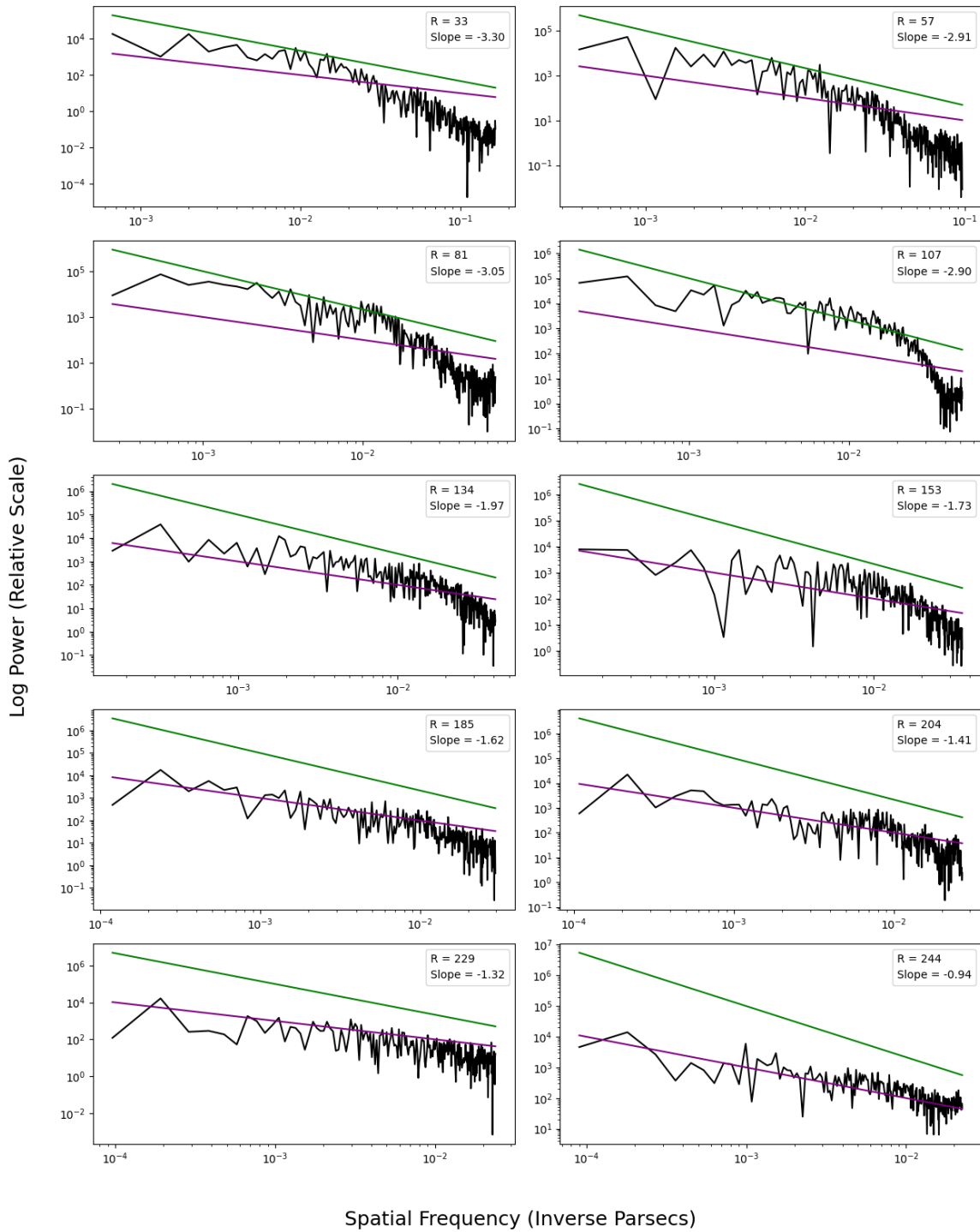


Figure 2.6: Power spectra obtained from different radial values showcasing known turbulence characteristics. The purple line has a slope of -1 , while the green line has a slope of $-5/3$.

in these regions. These nuanced deviations from the expected -5/3 slope highlight the intricate nature of galactic structures and the need for further exploration to comprehensively understand the underlying mechanisms shaping the structure of NGC 628.

Conclusion

After performing cloud counting and Fast Fourier Transform on JWST image data of NGC 628, patterns exhibiting behavior consistent with interstellar clouds formed by turbulence are observed. The study is conducted using emission data from the galaxy as opposed to analyzing its absorption data as in the comparative studies. The resulting fractal dimension of $D = 0.69 \pm 0.13$ from the cloud counting analysis aligns with that of galaxies whose disks are shaped by turbulence. The FFT power spectra exhibit slopes of approximately $-5/3$ for larger radii, aligning with expectations from turbulence studies. Deviations from the anticipated $-5/3$ slope for smaller radii suggest a different structural behavior or scale characteristic within these regions, warranting further investigation.

Further experiments may employ other techniques such as conducting spectral line observations to gain insights into the distribution, movement, and interaction of gas within the galaxy, utilizing simulations for modeling turbulence effects, and comparing NGC 628 with similar galaxies to broaden our understanding of turbulence's role in shaping galactic structures.

Appendix

A.1 Azimuthal Scans

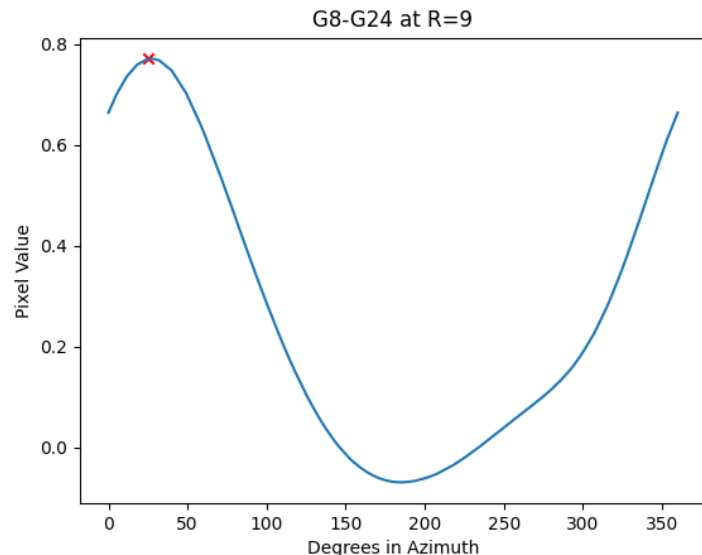


Figure A.1: Azimuthal scan at radius of 9 pixels for G8-G24 image.

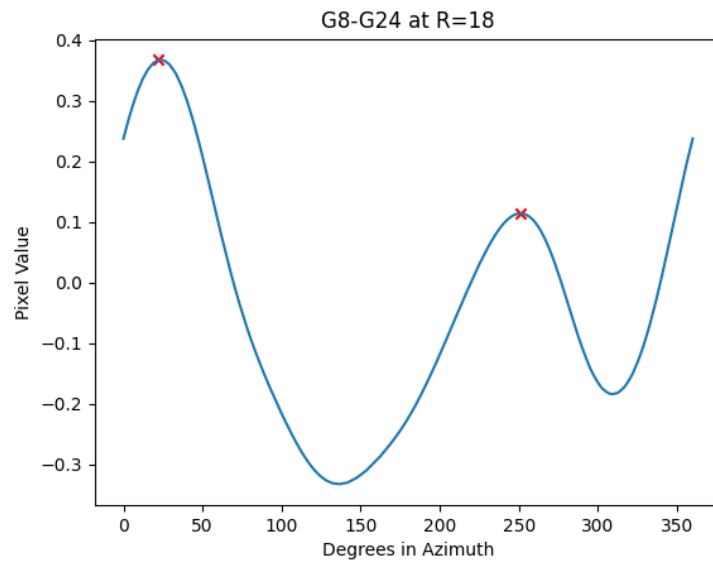


Figure A.2: Azimuthal scan at radius of 18 pixels for G8-G24 image.

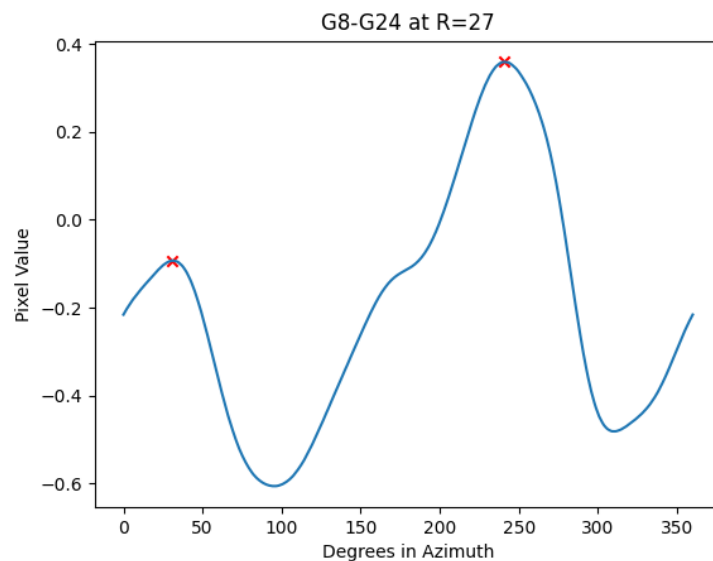


Figure A.3: Azimuthal scan at radius of 27 pixels for G8-G24 image.

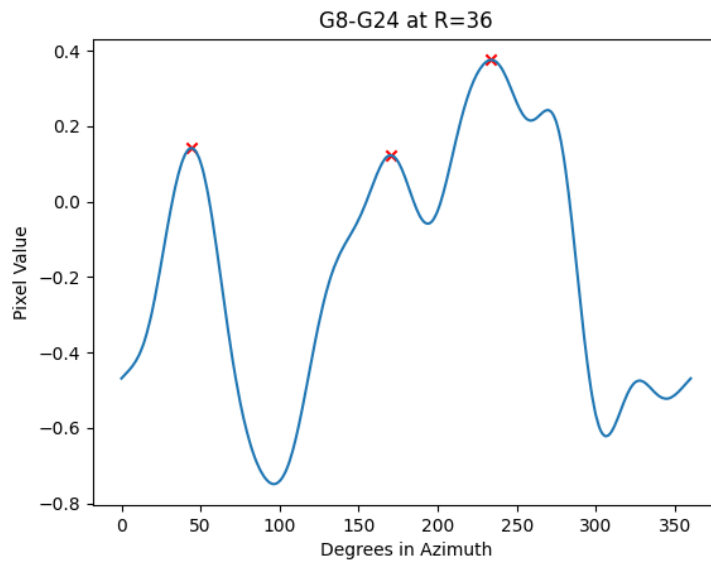


Figure A.4: Azimuthal scan at radius of 36 pixels for G8-G24 image.

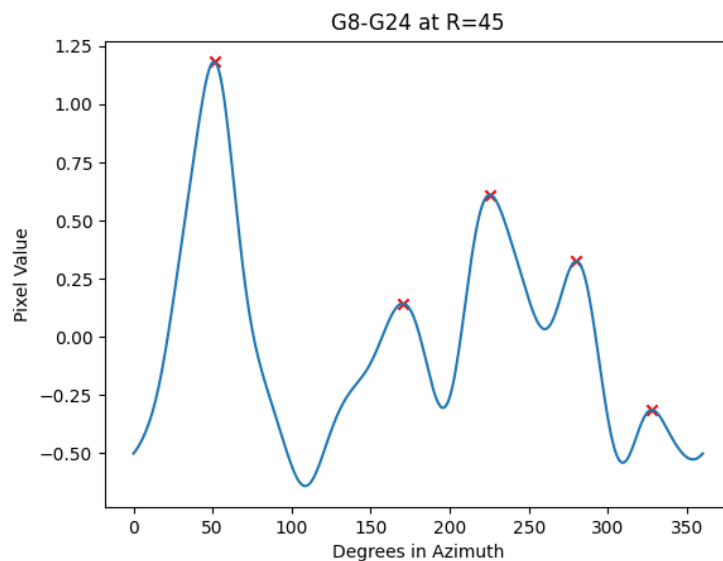


Figure A.5: Azimuthal scan at radius of 45 pixels for G8-G24 image.

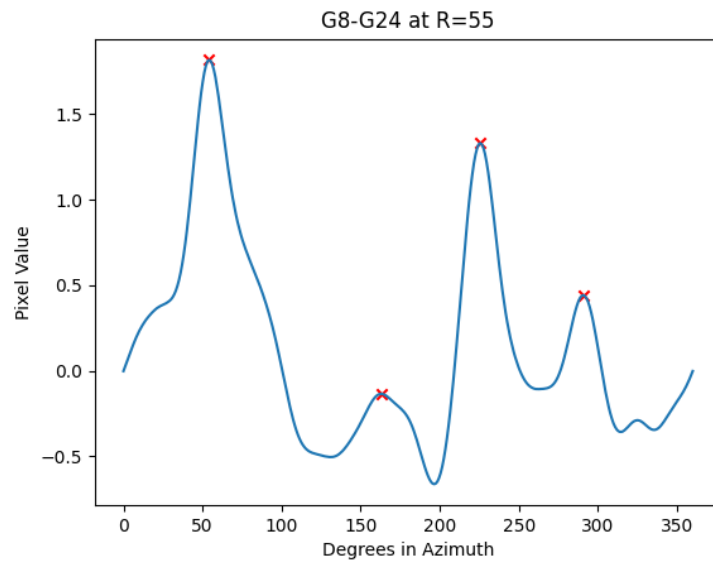


Figure A.6: Azimuthal scan at radius of 55 pixels for G8-G24 image.

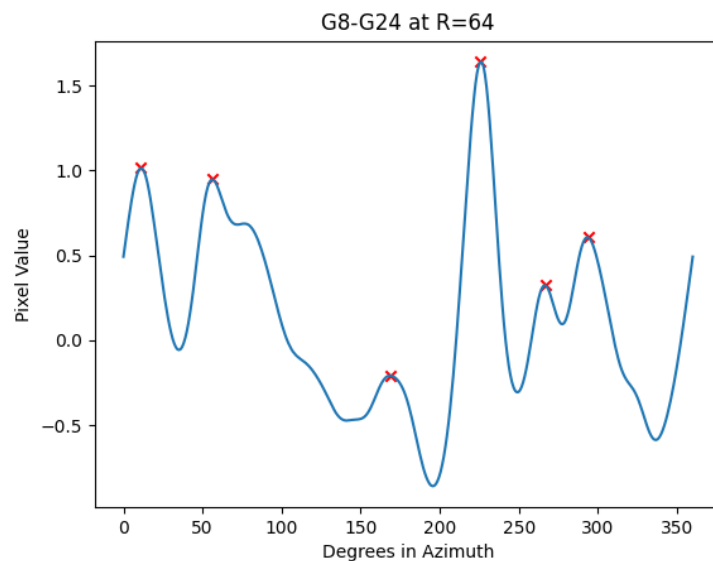


Figure A.7: Azimuthal scan at radius of 64 pixels for G8-G24 image.

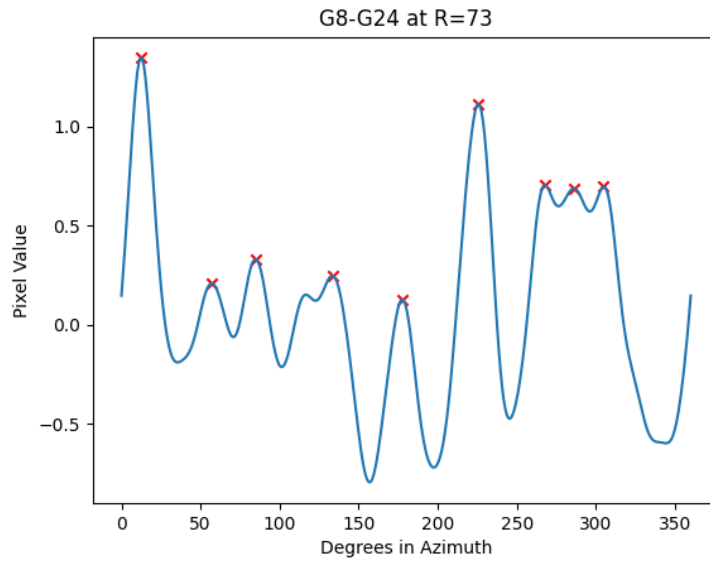


Figure A.8: Azimuthal scan at radius of 73 pixels for G8-G24 image.

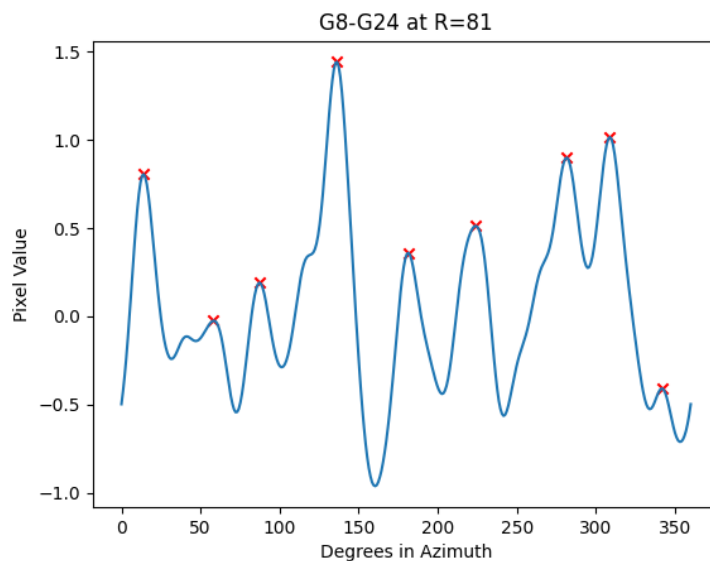


Figure A.9: Azimuthal scan at radius of 81 pixels for G8-G24 image.

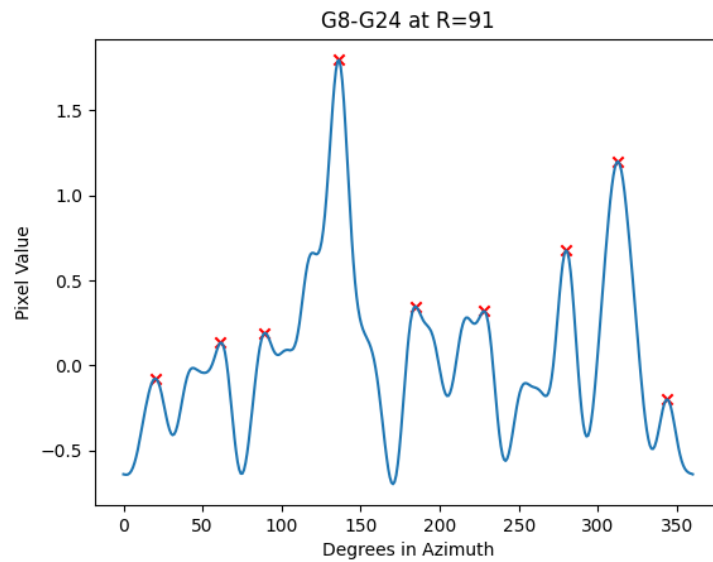


Figure A.10: Azimuthal scan at radius of 91 pixels for G8-G24 image.

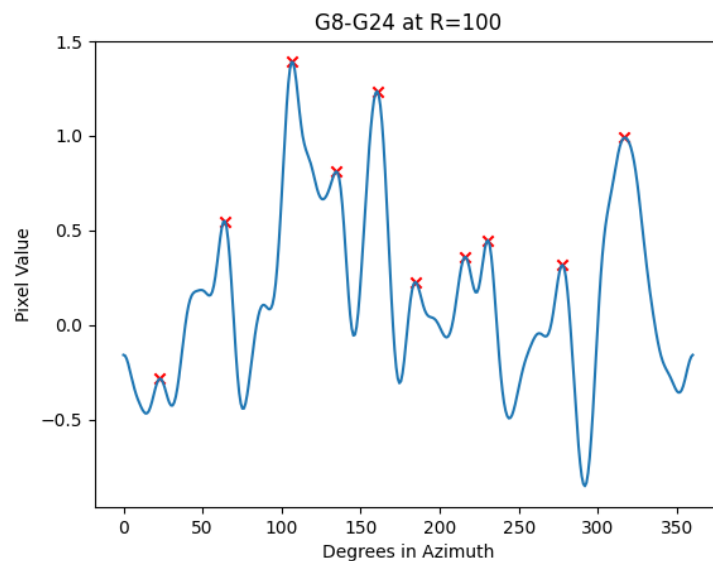


Figure A.11: Azimuthal scan at radius of 100 pixels for G8-G24 image.

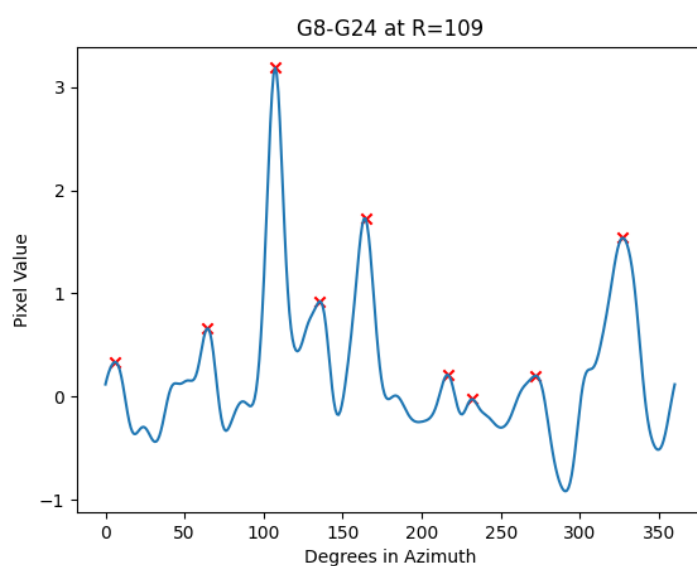


Figure A.12: Azimuthal scan at radius of 109 pixels for G8-G24 image.

A.2 Dust Spiral Counts

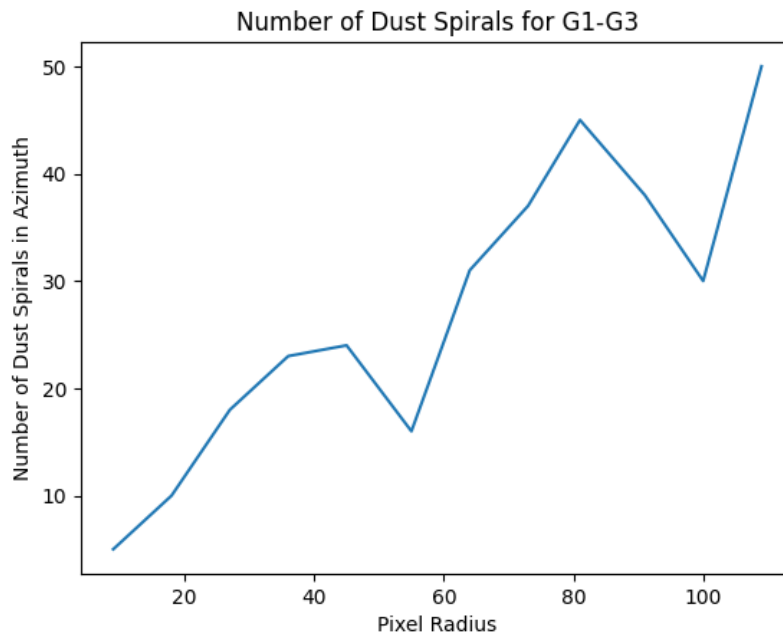


Figure A.13: Number of dust spirals detected for the G1-G3 difference along image radii.

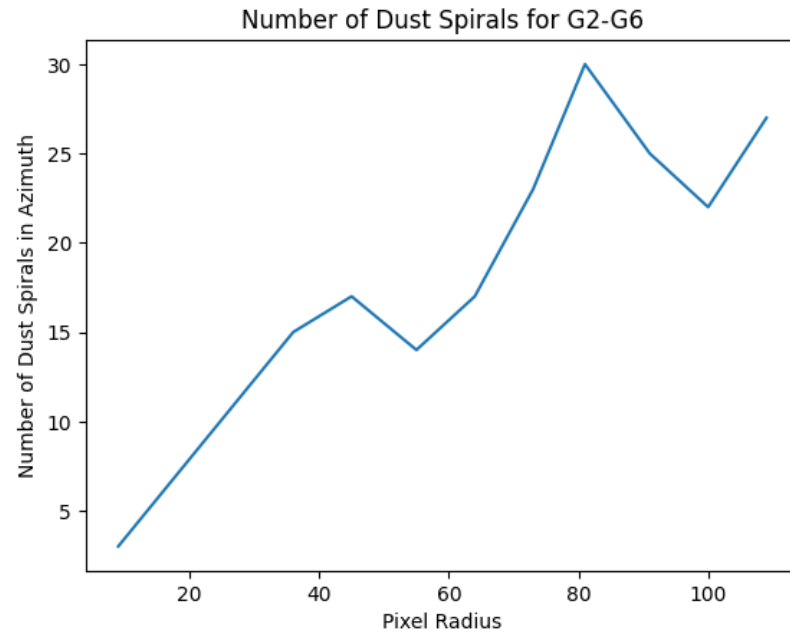


Figure A.14: Number of dust spirals detected for the G2-G6 difference along image radii.

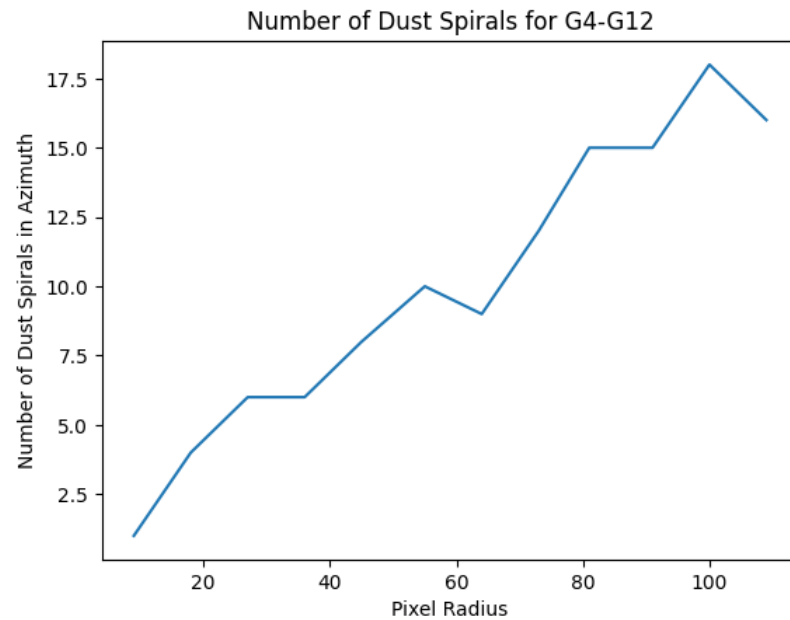


Figure A.15: Number of dust spirals detected for the G4-G12 difference along image radii.

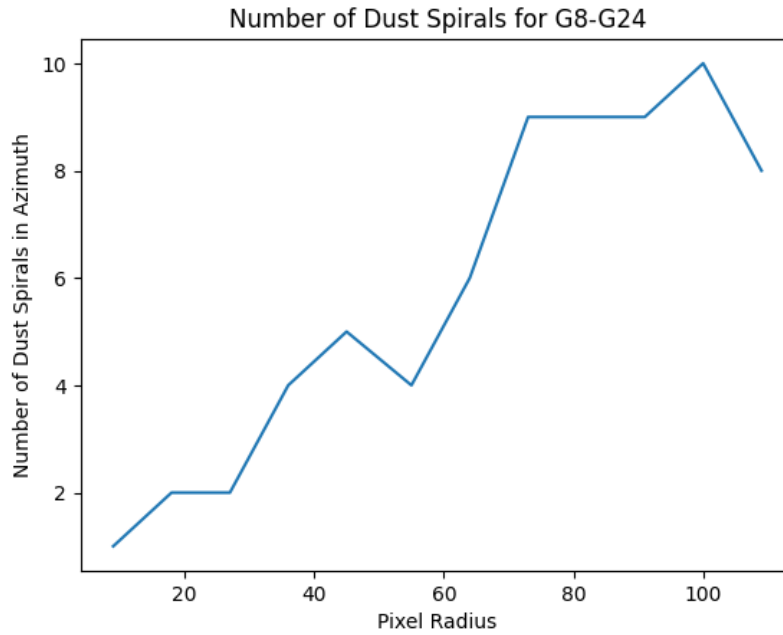


Figure A.16: Number of dust spirals detected for the G8-G24 difference along image radii.

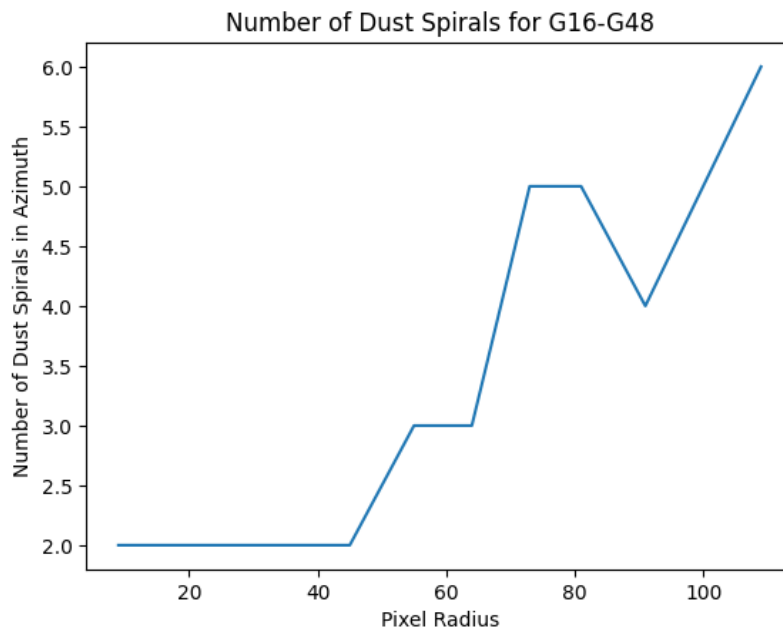


Figure A.17: Number of dust spirals detected for the G16-G48 difference along image radii.

Bibliography

- ¹A. Davis, A. Nierenberg, A. Peter, C. Garling, J. Greco, C. Kochanek, D. Utomo, K. Casey, R. Pogge, D. Roberts, D. Sand, and A. Sardone, *The lbt satellites of nearby galaxies survey (lbt-song), The satellite population of ngc 628*, 2021.
- ²P. Schneider, *Extragalactic astronomy and cosmology, An introduction* (Springer Berlin, Heidelberg, Germany, 2015).
- ³A. Tsinober, *An informal conceptual introduction to turbulence* (Springer, 2009).
- ⁴Z. Warhaft, *The engine and the atmosphere: an introduction to engineering* (Cambridge University Press, 1997).
- ⁵D. S. Viswanath, T. K. Ghosh, D. H. L. Prasad, N. V. Dutt, and K. Y. Rani, *Viscosity of liquids, Theory, estimation, experiment, and data* (Springer, 2007).
- ⁶G. Elert, *Viscosity* (2020).
- ⁷F. Argoul, A. Arneodo, G. Grasseau, Y. Gagne, E. Hopfinger, and U. Frisch, “Dusty acoustic turbulence in the nuclear disks of two liner galaxies ngc 4450 and ngc 4736”, *Nature* **338**, 51–53 (1989).
- ⁸B. G. Elmegreen and J. Scalo, “Interstellar turbulence i: observations and processes”, *Annual Review of Astronomy and Astrophysics* **42**, 2 (2004).
- ⁹D. M. Elmegreen, B. G. Elmegreen, and K. S. Eberwein, “Dusty acoustic turbulence in the nuclear disks of two liner galaxies ngc 4450 and ngc 4736”, *The Astrophysical Journal* **564**, 234 (2002).
- ¹⁰*About: frequently asked questions lite.*
- ¹¹*Jwst mid infrared instrument*, Aug. 2023.
- ¹²I. Procaccia, “Fractal structures in turbulence”, *Journal of Statistical Physics* **36**, 649–663 (1984).
- ¹³R. Xie, “Turbulence and its effect on star formation in galaxy ngc 524”, Undergraduate thesis (Reed College, 2020).